Journal of Environmental Chemical Engineering 12 (2024) 112670

Contents lists available at ScienceDirect

Journal of Environmental Chemical Engineering

journal homepage: www.elsevier.com/locate/jece

Cellulose nanofiber-templated metal-organic frameworks for fluorescent detection of methyl parathion pesticides

Kailong Zhang [a], Thomas Elder [b], Zhongyang Cheng [c], Ke Zhan [d], Yucheng Peng [d], Mi Li [a,*]

[a] Center for Renewable Carbon, School of Natural Resources, The University of Tennessee, Knoxville, TN 37996, USA
[b] USDA-Forest Service, Southern Research Station, Auburn, AL 36849, USA
[c] Materials Research and Education Center, Auburn University, Auburn, AL 36849, USA
[d] College of Forestry, Wildlife and Environment, Auburn University, Auburn, AL 36849, USA

ARTICLE INFO

Keywords:
Cellulose nanofibers
Metal-organic frameworks
Aggregation-induced emission
Luminescent sensor
Pesticide detection

ABSTRACT

Methyl parathion is a typical organophosphorus pesticide that poses threats to the global environment and human health. In this study, we developed a portable 2D sensing pad for monitoring methyl parathion based on the aggregation-induced emission (AIE) properties of an innovated hybrid material that integrates cellulose nanofibers (CNFs) with luminescent metal-organic frameworks (LMOFs). The hybrid material enhanced the flexibility and moldability of LMOFs and significantly improved the scalability of sensing material. The resulting CNF/LMOF material was shaped into a 2D pad, exhibiting fluorescent properties under UV exposure. The fluorescence of the pad was quenchable upon exposure to methyl parathion. This host-guest interaction enabled the precise quantification of the pesticide's concentration by monitoring the intensity variation of the fluorescence at 405 nm wavelength. We further engineered these hybrid pads into a user-friendly and portable sensing prototype, and then validated them with real sample testing. Time-dependent Density Functional Theory calculations were employed to elucidate the underlying fluorescence quenching mechanism triggered by methyl parathion. This work introduces a practical and sustainable sensing platform for pesticide detection.

1. Introduction

Methyl parathion, a widely used organophosphorus pesticide in agriculture, is effective in pest control but poses significant environmental and health concerns. Its pervasive application results in contamination of water sources and residual presence in agricultural produce [1,2]. Chronic exposure to methyl parathion may increase the risk of developing neurological disorders, such as Parkinson's disease [3]. The US Environmental Protection Agency (EPA) prohibits the use of methyl parathion on children's food crops but allows it on certain crops like fruits, vegetables, nuts, and grains, with limits ranging from 0.1 to 1 mg/L [4]. Currently, the detection of methyl parathion predominantly relies on techniques such as chromatography and spectrometry [5,6]. Although these methods are generally reliable and accurate, they are often labor-intensive and time-consuming, and they also necessitate specialized equipment. This complexity presents significant challenges for convenient and rapid detection of methyl parathion pesticides.

The limitations of current detection technologies have prompted the exploration of innovative functional materials, with metal-organic frameworks (MOFs) emerging as particularly promising options. MOFs are a class of porous crystals that are often synthesized through the assembly of metal ions coordinated with organic ligands [7]. They have demonstrated significant potentials in the detection of environmental pollutants through fluorescence sensing [8–10]. A notable subset of these MOFs incorporates ligands with aggregation-induced emission (AIE) properties to afford fluorescent sensing capabilities [11]. AIE molecules are a group of organic compounds that are known for their enhanced fluorescence upon aggregation [12]. The AIE molecules can act as ligand precursors to be integrated into the MOFs by coordinating active phenyl groups in the AIE ligands with metal ions [13,14]. AIE-based MOFs have demonstrated effectiveness in pesticide detection due to their highly porous structure and customizable properties [15]. For example, a europium-based MOF was constructed by integrating AIE-active molecules, demonstrating high sensitivity as a fluorescent sensor to detect phosphate and organic salicylaldehyde [16]. Despite their effectiveness, the detection of pesticides using MOFs is primarily conducted in aqueous environments. This is because MOFs conventionally synthesized through solvothermal methods exist as crystalline

* Correspondence to: University of Tennessee, 2506 Jacob Dr., Knoxville, 37996, TN.
E-mail address: mli47@utk.edu (M. Li).

https://doi.org/10.1016/j.jece.2024.112670
Received 28 January 2024; Received in revised form 26 March 2024; Accepted 30 March 2024
Available online 3 April 2024

powders, typically with a size of less than 10 μm [17,18]. As a result, it is challenging to fabricate these MOFs into portable detection devices at the macroscale with two- or three-dimensional (2D/3D) architecture.

Cellulose is a promising polymer substrate for templating MOFs due to its natural abundance, biodegradability, chemical modifiability, and low thermal expansion coefficient, which provides an attractive solution for compounding MOFs, offering moldability and 3D architecture [19]. The 2,2,6,6-tetramethyl-1-piperidinyloxy (TEMPO)-mediated oxidation is a prevalent method for modifying cellulose to make it suitable for MOF templating. This modification introduces carboxylate groups onto the surface of cellulose fibers [20]. These carboxylate groups can anchor the metal precursors in MOFs through coordination, thus allowing the subquently assembly and crystal growth of MOFs along the cellulose surface [21]. Moreover, the metal components act as a bridge to connect the AIE fluorophores and the cellulose substrate. This process not only strengthens the connection between cellulose and the fluorophore but also allows the AIE-based MOFs to adopt a macro-scale structure by leveraging the polymer features of cellulose [22]. Combining cellulose nanofiber (CNF) and AIE-based MOFs could be a promising strategy for designing a portable sensing platform for rapid and convenient detection of pesticides.

In this study, we used TEMPO-oxidized CNF (TOCNF) as a polymeric scaffold to template the *in situ* synthesis of a luminescent MOF (LMOF), which comprises zirconium ions and the organic linker 1,2,4,5-tetrakis (4-carboxyphenyl) benzene (H4TCPB) that possesses AIE properties. The TOCNF/LMOF hybrid exhibits blue luminescence under UV light. By combining the functions and features of both cellulose and MOFs, we developed a 2D hybrid pad that can serve as a portable sensing prototype for methyl parathion detection and quantification. Lastly, we employed Density Functional Theory (DFT) calculations to unravel the underlying sensing mechanism at the molecular level. Our study of the TOCNF/LMOF hybrid provides a technique for developing cost-effective, sustainable, and user-friendly sensing platforms for monitoring methyl parathion in the agricultural sector.

2. Materials and methods

2.1. Materials

CNF was purchased from the University of Maine with a concentration of 3.1 *wt*%. Sodium bromide (NaBr), sodium hypochlorite (NaClO), 2,2,6,6-tetramethyl-1-piperidinyloxy (TEMPO), zirconium chloride ($ZrCl_4$), benzoic acid, dimethylformamide (DMF), methyl parathion, rhodamine 6 G, and the interference chemicals, including nitrobenzene, glucose, sodium chloride, potassium chloride, and ferric chloride, were purchased from Fisher Scientific. The 1,2,4,5-tetrakis(4-carboxyphenyl) benzene (H4TCPB) was obtained from Millipore Sigma. All chemicals used in the study were of analytical grade and used as received.

2.2. Preparation of TOCNF

TOCNF was prepared according to the previously reported method with some modifications [23]. In this process, 1 L unmodified CNF suspension (1 *wt*%) was mixed with 150 mg TEMPO and 1.5 g NaBr. The pH of the resultant mixture was adjusted to 10.5 using 0.5 M NaOH or 0.1 M HCl. The reaction was initiated by adding 25 mmol of NaClO. The mixture was then stirred at 150 rpm at room temperature for 5 hours. Throughout this period, the pH was maintained at 10.5 using 0.5 M NaOH. The reaction was subsequently quenched by the addition of 50 mL ethanol. The resultant oxidized CNF product was washed with water thoroughly by filtration. Subsequently, the retentate was subjected to dispersion through a high-speed homogenizer (IKA Ultra-Turrax) at 10000 rpm for 30 minutes. The resulting TOCNF was then collected as the supernatant following centrifugation at 12000 g for 20 minutes. The carboxylate content of the TOCNF was determined to be 0.7 mmol/g using the electric conductivity titration method [24].

2.3. Preparation of LMOF and TOCNF/LMOF hybrid pad

The pristine LMOF was synthesized in accordance with a previous method [25]. Three LMOFs with varying concentrations of precursors, namely LMOF-a, LMOF-b, and LMOF-c from low to high, were prepared. In a 30 mL DMF solution, 16.67 mg $ZrCl_4$, 23.3 mg H4TCPB, and 0.9 g benzoic acid were added for the preparation of LMOF-a; 50 mg $ZrCl_4$, 70 mg H4TCPB, and 2.7 g benzoic acid were mixed for LMOF-b; 150 mg $ZrCl_4$, 210 mg H4TCPB, and 8.1 g benzoic acid were mixed for LMOF-c. The resultant mixtures were then maintained at 121 ℃ for 2 hours in an autoclave for reaction. After that, the LMOFs were collected by centrifugation at 10000 g for 10 minutes and subsequently washed twice with DMF followed by three washes with DI water using centrifugation.

To fabricate TOCNF/LMOF hybrids, 100 mL of 0.5 *wt*% TOCNF water suspension was mixed with 10 g $ZrCl_4$ followed by 30 minutes of stirring. The mixture was then purified through two rounds of washing with DI water and two rounds with DMF, using centrifugation at 10000 g for 10 minutes each. The purified TOCNF was redispersed in DMF to achieve a concentration of 0.5 *wt*%. Subsequently, 30 mL of the above suspension was mixed with $ZrCl_4$, H4TCPB, and benzoic acid, all in concentrations equivalent to those used in LMOF-a, LMOF-b, and LMOF-c, respectively. This resulted in the formation of TOCNF/LMOF hybrid-a, hybrid-b, and hybrid-c. The reaction conditions were the same as those employed for the pristine LMOFs. After the reaction, the TOCNF/LMOF hybrids were purified through two washes with DMF and three washes with DI water, using centrifugation at 10000 g for 10 minutes for each wash. The resultant hybrids were then redispersed in 30 mL DI water. Subsequently, aliquots of 10 mL from each suspension were filtered through a quantitative filter paper (Whatman) with an effective diameter of 47 mm. The retentate was dried in an oven at 40 ℃ for 24 hours. Upon drying, the resulting films (with respective thicknesses of 70 μm for hybrid-a, 100 μm for hybrid-b, and 110 μm for hybrid-c) were cut into circular pads with a diameter of 6 mm.

2.4. Characterization

The micromorphology of the LMOFs and hybrids was investigated using a scanning electron microscope (SEM) equipped with an energy-dispersive X-ray spectrometer (EDS) system (Zeiss). The samples were sputtered with gold prior to observation. The crystallinity was assessed using an X-ray diffractometer (XRD, PANalytical Empyrean) operating at 40 kV and 40 mA. The diffractograms were obtained at a scan rate of $4^\circ \bullet min^{-1}$ and a step size of 0.02°. Attenuated total reflectance-Fourier transform infrared (ATR-FTIR) spectroscopy (PerkinElmer) was used to collect spectra over the range of 400–4000 cm^{-1}, with a resolution of 4 cm^{-1}. The Brunauer-Emmett-Teller (BET) specific surface area was determined using N_2 adsorption-desorption isotherm measurements (Micromeritics TriStar II Plus). Approximately 15 mg of each sample was degassed under vacuum at 100 °C for one hour before measurement. The N_2 adsorption isotherms were recorded at 77 K. The fluorescence was determined using a microplate reader (Synergy H1) with an excitation wavelength of 290 nm. This wavelength is slightly lower than the absorption peaks of LMOF (Fig. S1), ensuring an adequate separation between the excitation wavelength and the maximum emission wavelength of 405 nm. The samples' photographs were taken with a digital camera under white light or UV light (300 nm).

2.5. Determination of quantum yield

The relative quantum yields of LMOF-b and hybrid-b were measured using rhodamine 6 G as a reference that has a known quantum yield of 94% in water when excited at 480 nm. The test samples were excited at 290 nm and the relative quantum yield was calculated using the equation [26]:

$$\Phi_T = \Phi_R \frac{Grad_T}{Grad_R}\left(\frac{n_T}{n_R}\right)^2$$

where Φ is the quantum yield, the subscript R refers to the rhodamine 6 G reference, and subscript T refers to the test sample, and Grad is the gradient of the linear fit obtained from the plot of integrated fluorescence intensity versus absorbance. The gradients were determined based on five different concentrations of rhodamine 6 G and the test samples, respectively. Both the reference and test samples were measured in water in which the refractive index ratio (n_T/n_R) equals to 1.

2.6. Detection and quantification of methyl parathion

To assess the efficiency of the hybrid pads in detecting methyl parathion, each hybrid pad was immersed in 4 mL of methyl parathion solutions with varying concentrations. The immersion period was fixed at 10 minutes. After immersion, the fluorescence of the pads was measured using a microplate reader with an excitation wavelength of 290 nm. The quenching ratio was calculated as the reduced fluorescence intensity of the pad after quenching in methyl parathion solution to the fluorescence intensity of the unexposed pad soaking in DI water (without methyl parathion). The quenching ratios derived from various concentrations of methyl parathion were used alongside their respective methyl parathion concentrations to establish a standard curve.

Samples of tap water, Tennessee River water collected at Knoxville TN, and orange juice were selected to validate the detection efficiency. The tap water and river water samples were centrifuged at 4000 g for 10 minutes. The supernatant was spiked with 0.2, 0.5, and 2 mg/L methyl parathion. The orange juice was extracted from fresh oranges purchased at a local market using a juicer, and then diluted 50 times with DI water. The juice sample was spiked with 0.2, 0.5, and 2 mg/L methyl parathion and treated with acetonitrile following the previous method [27]. The hybrid pads were immersed in these spiked solutions and their fluorescence intensity was determined using the method discussed above. The concentrations were derived from the fluorescence intensity using the established standard curve.

2.7. Theoretical calculations

The theoretical calculations were conducted using the Gaussian 16 software suite. DFT and time-dependent DFT (TD-DFT) were used in these computations. The PBE0 functional was selected in combination with the 6–311+G(d,p) basis set for all calculations. Initial geometry optimization was performed for both the ground and first excited states of the molecules. TD-DFT calculations were performed using the optimized ground state geometry as a basis for probing electronic excitations. Additionally, the TD-DFT employed the optimized first excited state geometry to elucidate properties relevant to the emission. The empirical dispersion correction was incorporated, and the solvent effect of water (polarizable continuum model) was considered to represent the molecular behavior in an aqueous environment.

3. Results and discussion

3.1. Material characterization

We synthesized three pristine LMOFs with varying morphological appearances by modulating the concentrations of the metal and ligand precursors. The geometry and size of the LMOF crystals correlated with the precursors' concentrations: the lowest concentration produced the smallest and spheric particles of LMOF-a, with diameters under 100 nm (Fig. 1**A**). The intermediate precursors' concentration resulted in the LMOF-b particles, exhibiting a spheric shape with diameters around 300 nm (Fig. 1**B**). The highest precursor concentration led to an oval shape and the largest LMOF-c particles with diameters of 1–2 μm (Fig. 1**C**). The precursors' concentration in the synthesis mixture is a

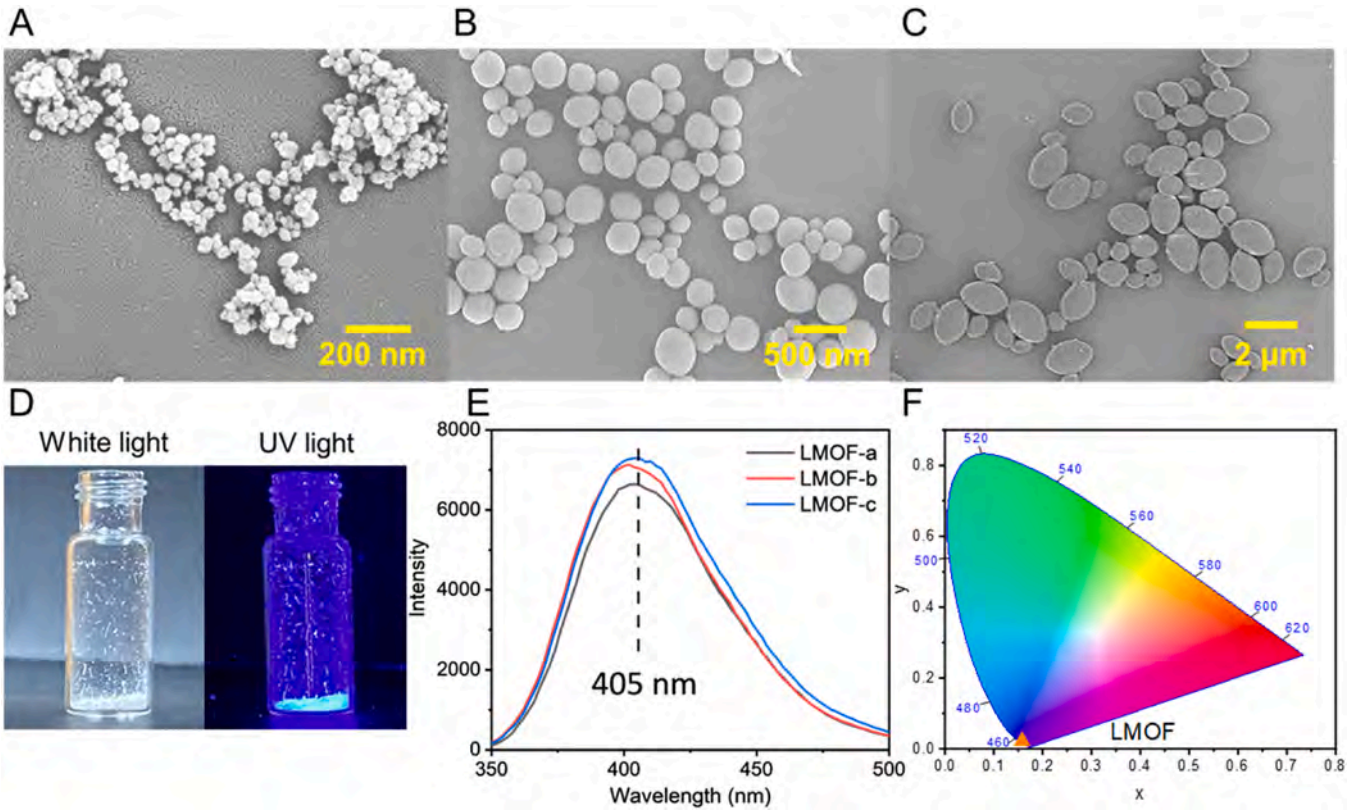

Fig. 1. Characterization of LMOFs. SEM images of LMOF-a, LMOF-b, and LMOF-c (A-C). Visual appearance of LMOF-b particles under white and UV light (D). Fluorescentce spectra of LMOF-a, LMOF-b, and LMOF-c, with each concentration adjusted to 0.5 mg/L (E). CIE color coordinates (F).

critical factor that influences the particle size and geometry of the resultant LMOFs. An increase in precursor concentration boosts the diffusion rates and the coordination probability, thereby promoting the crystal growth and the formation of larger particles [28]. During the synthesis, the carboxylate groups in the H4TCPB ligands coordinate with the zirconium ions, forming a structure with SCU topology [29]. The benzoic acid serves as a modulating agent to tune the size and morphology of the LMOF particles. Benzoic acid can selectively occupy certain coordination sites on the zirconium, thereby influencing the overall coordination environment and guiding the assembly of the LMOFs [29].

All three LMOF particles exhibited fluorescent properties. Under white light, the LMOFs appeared as white crystalline powders (Fig. 1**D**). When exposed to UV radiation, the LMOFs emitted blue light at a wavelength of 405 nm, and the fluorescence intensity was consistent across all three LMOFs when their concentrations were adjusted to the same level (0.5 mg/L, Fig. 1**E**). This suggests the fluorescence intensity is quantifiable and independent of the original concentration used for the synthesis and geometry of the LMOFs. The fluorescence corresponds to CIE 1931 color coordinates of x = 0.15 and y = 0.06 (Fig. 1**F**).

TOCNF was used as a supporting substrate to template the LMOF crystals, thereby conferring their structural patterns at a macroscopic level. As illustrated in Fig. 2**A**, the TOCNF exhibited a fibrous morphology with a length of several microns and a diameter of less than 10 nm. The nanoscale dimensions of TOCNF are well-suited to align with the LMOF particles, offering geometric compatibility for compounding and templating. We combined the TOCNF with the LMOF precursors—Zr^{4+} and the H4TCPB ligand—to achieve the *in situ* hybridization of TOCNF and LMOFs via a one-pot synthesis approach. During this synthesis, the carboxylate groups on the TOCNF surface act as binding sites for the Zr^{4+} ions. The interaction between TOCNF and Zr^{4+} initiates the nucleation of the LMOF crystals. Prior studies have elucidated that the assembly between carboxylate groups and zirconium atoms was characterized by a distinctive coordination pattern around the zirconium center. Within the local coordination environment, the equatorial coordination sphere of the zirconium atom comprised two oxide ions, two hydroxide ions, two oxygen atoms from carboxylate groups, and two water molecules. The bond distance between the zirconium and the oxygen atoms of the carboxylate ligands ranged from 2.16 to 2.28 Å [30]. This suggests a strong bond formed between the TOCNF and the zirconium within the LMOF. The SEM images revealed that the LMOF particles were evenly distributed along and affixed to the TOCNF surface (Fig. 2**B-D**). The LMOFs in the hybrids retained the size distribution characteristic: the particle size exhibited a proportional increase as the concentrations of the precursors increased, as shown in Fig. 1**A-C**. Subsequent EDS mapping of TOCNF/LMOF hybrid-b showed a uniform dispersion of zirconium element (Fig. S2A), indicating that the zirconium-based MOFs were evenly assembled on the cellulose surface. The crystalline structures in the TOCNF/LMOF hybrids were characterized through powder XRD analysis (Fig. S2B). The XRD pattern of TOCNF exhibited peaks corresponding to the crystallographic planes of cellulose at 2θ of 16.5° and 22.5° [31]. Notably, the diffraction peaks of TOCNF were significantly less intense than those of LMOF, which is attributed to the inherently lower crystallinity of the organic fibers compared with the LMOFs. The XRD pattern revealed distinct peaks at 2θ values of 7.2, 8.9, 10.3, and 11.5°, which are characteristic peaks of the zirconium-based LMOF [25]. This result confirms the preservation of the LMOF crystalline phase on the TOCNF substrate. The FTIR absorbance peaks at 3340 and 1057 cm^{-1} in TOCNF corresponded to the streching of the hydroxyl groups and the C-O of cellulose, respectively (Fig. S2C). Upon the incorporation of LMOF, there was a noticeable decrease in the intensity of these characteristic TOCNF peaks. Additionally, the peaks at 1606 and 1415 cm^{-1} were attributed to the carboxylate groups present in the H4TCPB ligand and TOCNF. The peaks at 860 and 782 cm^{-1} were ascribed to the C-H bending in the aromatic benzene ring of the H4TCPB ligand. The peak at 650 cm^{-1} was ascribed to the streching of Zr-O, which indicates the metal-ligand interaction within the LMOF framework [25]. These spectroscopic analyses confirm that the TOCNF/LMOF maintains the characteristic features of both cellulose and LMOF. The BET specific surface area of LMOF-b was measured to be 1518 m^2/g, and the total pore volume was calculated to be 0.6 cm^3/g (Fig. S3). The high surface area is attributed to the reticular topological connection between the metal nodes and the organic ligands in the LMOF structure. This porisity is in accordance with previously reported values for zirconium and H4TCPB MOFs [25]. Upon hybridization with TOCNF, the BET specific surface area of the hybrid-b sample

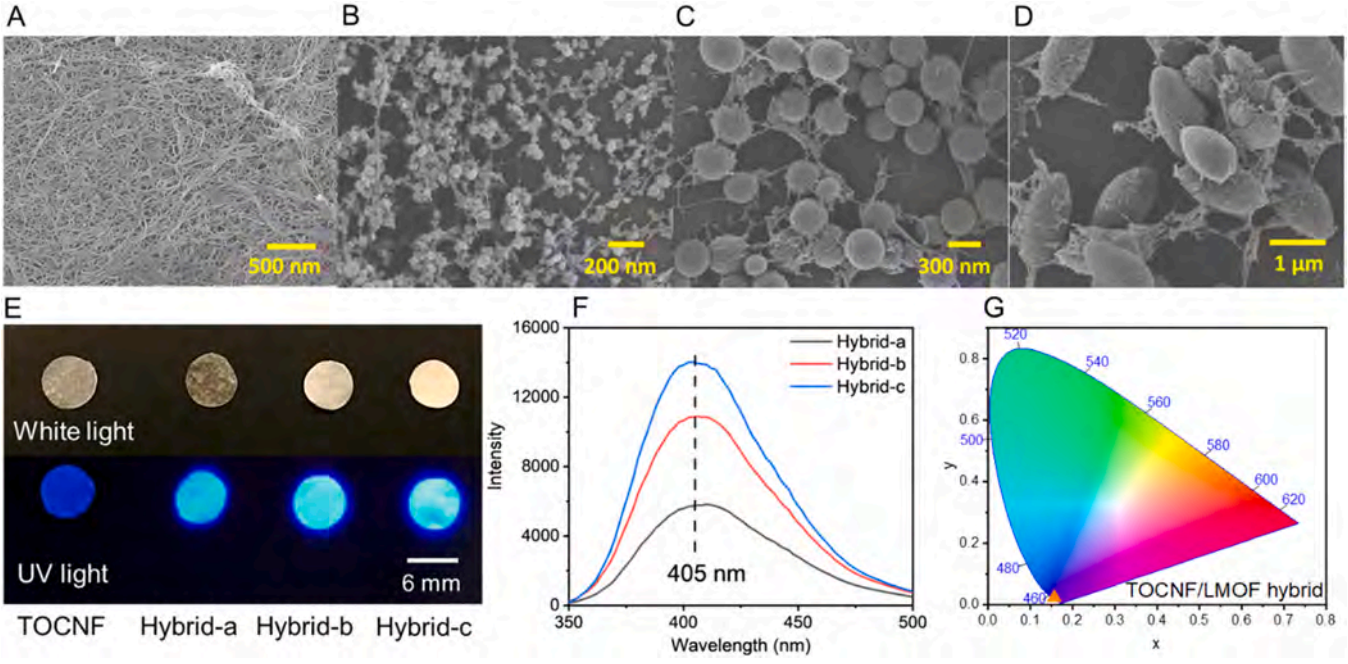

Fig. 2. Characterization of TOCNF/LMOF hybrids. SEM image of TOCNF (A). SEM images of TOCNF/LMOF hybrid-a, hybrid-b, and hybrid-c (B-D). Visual appearance of TOCNF and hybrid pads under white and UV light (E). Fluorescence spectra (F). CIE color coordinates (G).

was reduced to 782 m^2/g, and the pore volume was reduced to 0.41 cm^3/g, both of which are lower than those of the pristine LMOF-b. Despite the reduction of surface area caused by the TOCNF, the surface area of the hybrid remains significantly higher compared to high-porosity cellulose aerogels or conventional porous materials such as activated carbon [32,33]. The high surface areas of the hybrids are expected to provide ample available interactions for methyl parathion.

The integration of the TOCNF biopolymer with the LMOF enabled the fabrication of hybrid materials with tailored macroscale architectures. As illustrated in Fig. 2**E**, the TOCNF/LMOF hybrids can be shaped into 2D portable pads with a diameter of 6 mm. When subjected to UV light, these hybrids exhibited blue color, with the intensity increasing in proportion to the concentration of the precursors used for LMOF synthesis. This was also observed in the fluorescence spectra (Fig. 2**F**), where the hybrid-c exhibited the highest fluorescence intensity followed by hybrid-b, while hybrid-a showed the lowest. The emission peaks for all hybrids remained constant at 405 nm, with the chromaticity coordinates being x = 0.15 and y = 0.06 (Fig. 2**G**). These values were consistent with those observed for the pristine LMOF, indicating that the intrinsic fluorescent properties of the LMOF were preserved within the hybrid materials. The relative quantum yields of LMOF-b and hybrid-b were determined to be 26.6% and 37.8%, respectively, when excited at 290 nm. The hybridization with TOCNF increased the quantum yield of the LMOF-b. This enhancement is likely related to the absorption of radiation by the LMOF at 290 nm triggers the activation of radiative decay of TOCNF.

3.2. Sensing of methyl parathion

The efficacy of the three TOCNF/LMOF hybrid pads in sensing and quantifying methyl parathion was evaluated. Fig. 3 illustrates that each hybrid pad exhibited a distinct fluorescent response in intensity to the varying concentrations of methyl parathion. For all three pads, a progressive decline in fluorescence intensity was observed as the concentration of methyl parathion increased in the testing solution. However, the sensitivity levels of the hybrid pads were different. For instance, the fluorescence of the hybrid-a pad made from the lowest concentrations of precursors in LMOF was largely quenched at a concentration of 10 mg/L methyl parathion (Fig. 3**A**). In contrast, the concentrations for quenching hybrid-b and hybrid-c pads made from higher concentrations of precursors in LMOF were much higher, i.e., 20 mg/L or more (Figs. 3**B and** 3**C**). This variance could be attributed to the different loading portions of LMOFs within the hybrid pads. A higher concentration of precursors likely led to a larger proportion of LMOFs in the hybrid pad due to their larger crystal size, consequently increasing the number of interacting sites, which in turn influenced its sensitivity to methyl parathion.

We then selected hybrid-b pad to develop a portable sensing prototype for detecting the concentration of methyl parathion. To find out the minimum soaking time required for the hybrid to take in methyl parathion in solution, we performed a sensing kinetic analysis for the pad (thickness = 100 μm). The results indicated that the quenching effect reached an equilibrium after approximately 8 minutes when immersing the pad in 5 mg/L methyl parathion solution (Fig. S4). This implies that a specific duration is necessary for methyl parathion to diffuse and interact adequately within the hybrid pad. In the current study, the incorporation of the templating TOCNF substrate might cause a slight barrier impeding the immediate interaction between methyl parathion and LMOFs. This effect slightly reduced the rate (i.e., increase time) at which the sensor reached its maximum quenching efficiency. The soaking time for the sensing pad was then set at 10 minutes based on this result. Fig. S5 demonstrates that when soaking the hybrid-b pad in water, the fluorescence was mainly concentrated on the pad. The liquid part had negligible fluorescence. We then determined the fluorescence intensity of the supernatant, which showed that the intensity was almost identical from that of DI water. This result implies that the LMOF particles were securely bound to the hybrid pad, with no particle leaching during the immersion in water in the current procedure. This robust binding of LMOF with TOCNF likely benefits from the *in situ* synthesis process, where the carboxylate groups in the cellulose effectively interacted with the metal precursors of the LMOFs, enhancing the stability of the attachment [34]. Furthermore, the hybrid pad retained its 2D shape after immersion with moderate swelling (swelling ratio = 2.11 ± 0.22, defined as the weight increase of the pad post-immersion compared to its original weight before immersion). This observation indicates the pad's mechanical robustness and its ability to withstand water without significant deformation for future recovery.

We then soaked the sensing pad in 4 mL solution with analyte and employed fluorescent spectrometer to evaluate the sensing performance for methyl parathion. The quenching ratio, which refers to the proportional decrease in fluorescence intensity, was quantified across a range of methyl parathion concentrations from 0.05 to 20 mg/L (Fig. 4**A**). The sensor's response followed a linear trend within the lower concentration range of less than 5 mg/L. A linear relationship was established between the logarithmic values of concentration and the quenching ratio in the concentration range of 0.1–5 mg/L (Fig. 4**B**). This relationship was depicted by the regression curve with a R^2 of 0.995, indicating a high correlation between the quenching ratio and the methyl parathion concentrations. The linear relationship is described by the equation Log $y = 0.708 \text{ Log } x + 1.272$, where y represents the quenching ratio (%) and x is the concentration (mg/L) of methyl parathion. As depicted in Fig. 4**A**, a deviation from linearity with a decreasing gradient is observed beyond 5 mg/L of methyl parathion. At higher concentrations of analyte, the interactive sites of the pad become increasingly occupied, inhibiting further linear changes in fluorescence [35,36]. This deviation is likely related to different host-guest interaction kinetics, indicating a near-saturation of the active sites in the sensing pad. Therefore, this phenomenon indicates that the sensor's response is not suitable for

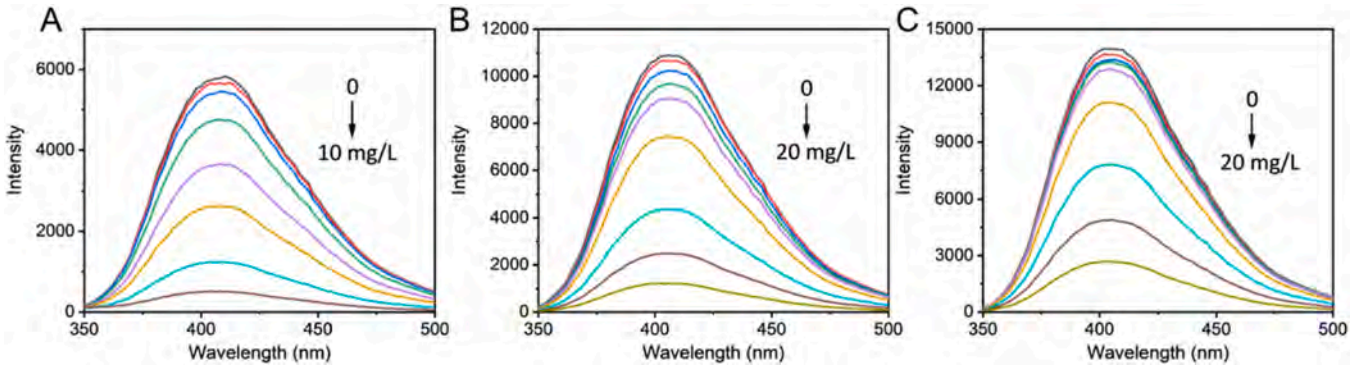

Fig. 3. Comparative fluorescence responses of TOCNF/LMOF hybrid pads to varying concentrations of methyl parathion. A: hybrid-a pad. B: hybrid-b pad. C: hybrid-c pad.

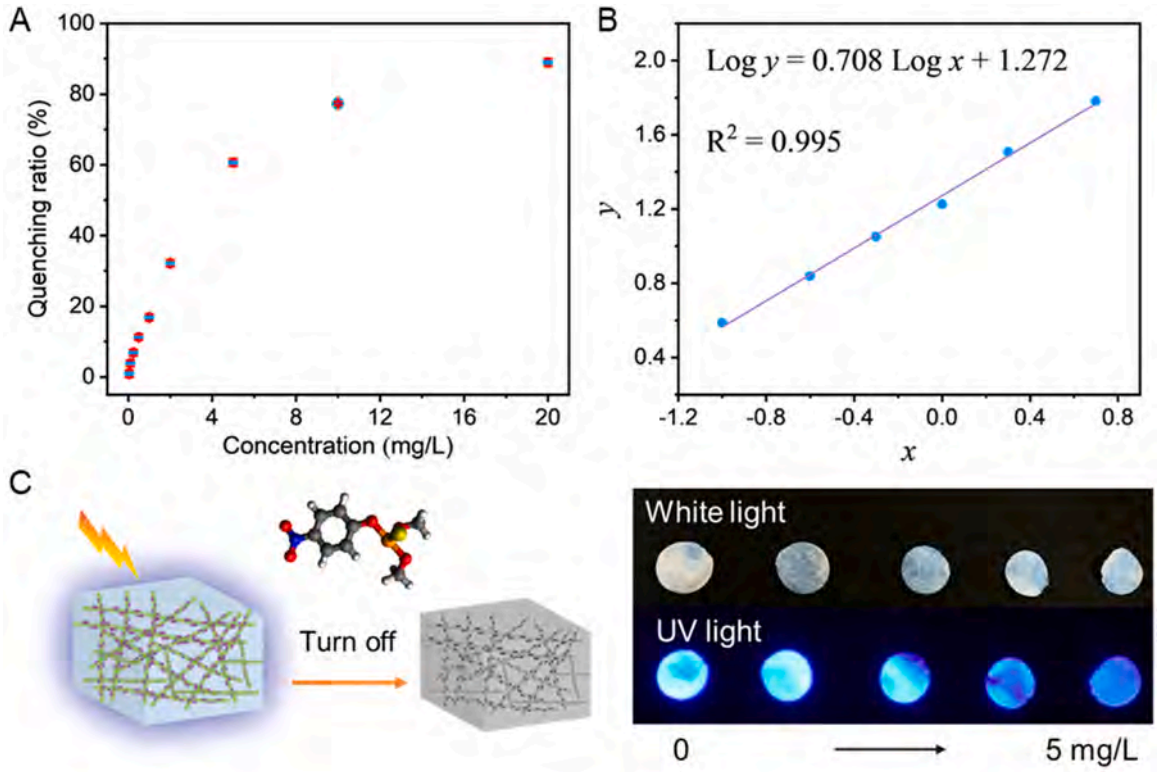

Fig. 4. Sensing performance of the hybrid-b pad for methyl parathion. Fluorescence quenching ratios at concentrations ranging from 0.05 to 20 mg/L (A). Linear relationship between the logarithms of x (concentration of methyl parathion, mg/L) and y (quenching ratio, %) (B). Illustration of quenching and photographs of the pad's response at concentrations of 0, 0.2, 1, 2, and 5 mg/L under white and UV light (C).

quantification when the analyte concentration is beyond the linear range (0.1 – 5 mg/L). We recommend that the testing samples be appropriately diluted to fall within the range of 0.1–5 mg/L for accurate quantification. Moreover, the fluorescence alteration was noticeable to the naked eye at concentrations exceeding 1 mg/L when exposed to UV light (Fig. 4**C**). This allows for a rapid estimation without the need for specialized equipment. The limit of detection (LOD) was calculated using the formula LOD = (3σ/S), where σ is the standard deviation of the blank signal response and S is the slope of the calibration curve [37]. The LOD for the hybrid pad was calculated to be 1.3×10^{-3} mg/L, which is comparable to other sensors reported in the literature [37–39]. As demonstrated in Fig. S6, the sensing pad exhibited high selectivity towards methyl parathion, with minimal interference from other chemicals such as nitrobenzene, glucose, and cations including Na^+, K^+, and Fe^{3+} [38]. These substances have negligible impact on the fluorescence quenching ratio of the hybrid pad.

We finally validated the practical effectiveness and reliability of the pad's sensing performance by testing samples in real conditions. We selected tap water, river water, and orange juice spiked with standard methyl parathion to reach concentrations of 0.2, 0.5, and 2 mg/L as test media to assess the performance of the sensing pads. The detected concentrations were calculated using the above established linear regression equation. As summarized in Table S1, the concentrations detected by our sensing prototype are closely aligned with the spiked concentrations. The observed recoveries of the three samples ranged from 93.0% to 108.1%. These results align closely with those obtained using the gas chromatography method [40]. The US EPA has set regulatory limits for the use of methyl parathion, allowing its presence in or on agricultural products within a concentration range of 0.1–1 mg/L [4]. Therefore, our results suggest that the newly developed hybrid pad is a viable tool for analyzing real samples containing methyl parathion.

3.3. Mechanism of sensing

In this study, the ligand H4TCPB in the LMOF is a chromophoric molecule with AIE properties. This molecule is characterized by its central benzene ring, which is linked with four carboxyphenyl groups (Fig. S7A). The structural arrangement of these groups constrains its intramolecular motion, enabling a radiative decay process when excited by photon energy [41]. The fluorescent property of the resulting LMOF is derived from the immobilization of the H4TCPB chromophore within its structure through coordination bonds. The integration of the ligand into the MOF's rigid framework limited the rotation and vibration of the phenyl rings, which inhibited the non-radiative decay pathways and in turn enhanced the fluorescence [13]. The free H4TCPB ligand itself showed a blue color when dispersed in water and exhibited an emission peak at 405 nm (Fig. S7B and S7C), demonstrating the inherent fluorescent property of the chromophore. This peak is identical to the maximum emission observed for the LMOF at 405 nm, suggesting that the LMOF demonstrated the AIE characteristics of the H4TCPB ligand.

We employed DFT calculations to investigate the mechanism behind the fluorescence quenching of methyl parathion. We initially optimized the ground-state geometry of H4TCPB/methyl parathion. As depicted in Fig. S8, an interaction formed between the nitro group of methyl parathion and the carboxyl group of H4TCPB ligand. The resulting O-H bond length was 1.895 Å, and the binding energy was calculated to be −0.73 eV. These results suggest that the H4TCPB ligand was energetically favorable to interact with methyl parathion. Further TD-DFT calculation was performed to probe the electronic aspects of this interaction. As shown in Fig. 5, the low-lying singlet electronic transition from the ground state (S0) to the first excited state (S1) of the H4TCPB ligand was predominantly composed of the highest occupied molecular orbital (HOMO) to the lowest unoccupied molecular orbital (LUMO) transition, accounting for 97.8% of the orbital contribution, and was

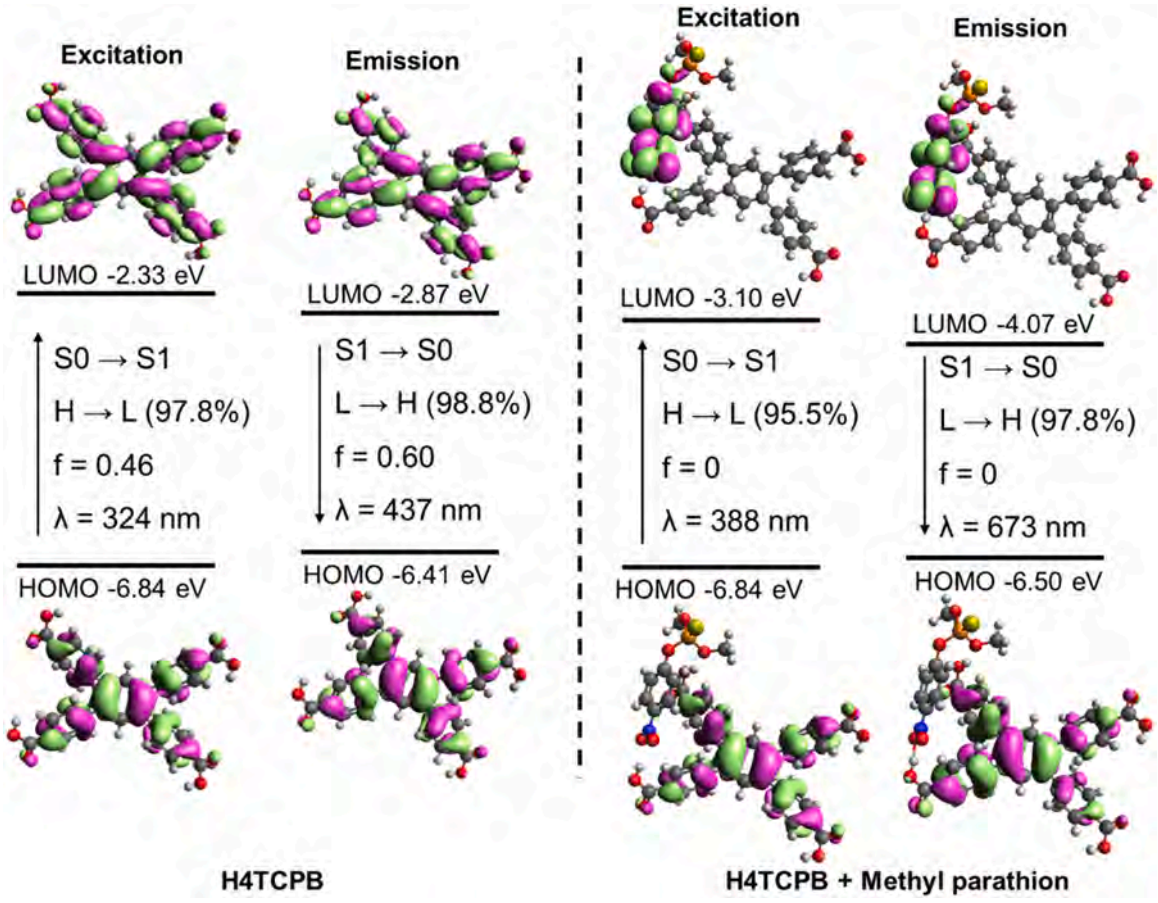

Fig. 5. Frontier molecular orbitals of the H4TCPB ligand and H4TCPB/methyl parathion complex in the vertical excitation and emission process.

characterized by an oscillator strength of f = 0.46. The oscillator strength quantifies the probability that an electron absorbs or emits photons, with a higher value indicating a higher probability of absorption or emission [42,43]. The energy values for the transitions from S0 to S1 were calculated to be 324 nm (3.83 eV). Examination of the frontier molecular orbitals of the H4TCPB ligands revealed that the electronic density of the HOMO orbitals was distributed throughout the entire molecular structure. The transition from S0 to S1 was characterized as a $\pi-\pi^*$ transition, with the p orbitals of carbon atoms playing a crucial role in the process [44]. In the emission process, the H4TCPB ligand exhibited emission at 437 nm (2.84 eV) with an oscillator strength of 0.60. This process corresponded to the LUMO to HOMO transition that accounted for 98.8% of the orbital contribution. The calculated energy value deviated only by 0.22 eV from the experimentally observed value of 405 nm (3.06 eV), demonstrating a concordance between the calculated and experimental emission spectra [45]. The S0 → S1 excitation in the H4TCPB/methyl parathion complex corresponded to a primary orbital transition from the HOMO to LUMO which contributed 95.5% of the total transition. This orbital transition exhibited a transfer in electronic density from the HOMO of the H4TCPB ligand to the LUMO of nitrobenzene group in methyl parathion. Such transition indicates that the methyl parathion could withdraw electrons from H4TCPB during excitation [45,46]. The calculated emission results for the H4TCPB/methyl parathion complex reveal an absence of fluorescence, as evidenced by the calculated emission at 673 nm (1.84 eV) and the oscillator strength of zero. This emission corresponded to a transition from the LUMO to HOMO, which constituted 97.8% of the orbital contribution. In addition, we investigated the excitation and emission process of the TOCNF. As detailed in Table S2, the calculated results reveal that both the TOCNF and the TOCNF/methyl parathion complex exhibited negligible emissions, as supported by the oscillator strength values that were close to zero. These computation results indicate that the methyl parathion quenched the fluorescence of H4TCPB via charge transfer.

We subsequently assessed the sensing capabilities of the AIE-based LMOF (referred to as LMOF-b in this section) in comparison to the H4TCPB ligand only. As depicted in Fig. 6**A**, there was a notable quenching of fluorescence intensity in the LMOF with increasing concentrations of methyl parathion. In contrast, the fluorescence intensity of the H4TCPB ligand displayed only a marginal decrease under similar conditions (Fig. 6**B**). Our DFT calculations provided insights that the methyl parathion can quench the fluorescence of H4TCPB by electron withdrawal. However, it is important to note that the efficiency of this quenching process is not determined entirely at the molecular level. The structural architecture of the material itself also plays a crucial role in influencing the quenching efficiency. The LMOF and the hybrid materials exhibited high BET specific surface areas, as shown in Fig. S3. Moreover, according to the structural model proposed by previous studies, the LMOF was characterized by a porous framework. The elementary unit of the framework included a rhombic channel with dimension of 5.3 × 10.5 Å, and a smaller pore on the lateral side with dimension of 2.4 × 3.5 Å [25]. Such features facilitate the diffusion of methyl parathion within the framework, allowing more extensive interaction with the LMOF (Fig. 6**A**). On the other hand, the pure H4TCPB ligand, despite its fluorescent properties, was less effective in sensing due to its aggregated state, which limited the availability of quenchable sites when exposed to methyl parathion (Fig. 6**B**). Therefore, the immobilization of H4TCPB into the LMOF not only maintained the fluorescence of the AIE-based ligand but also amplified its sensing abilities through enhanced interaction with the target analyte due to the

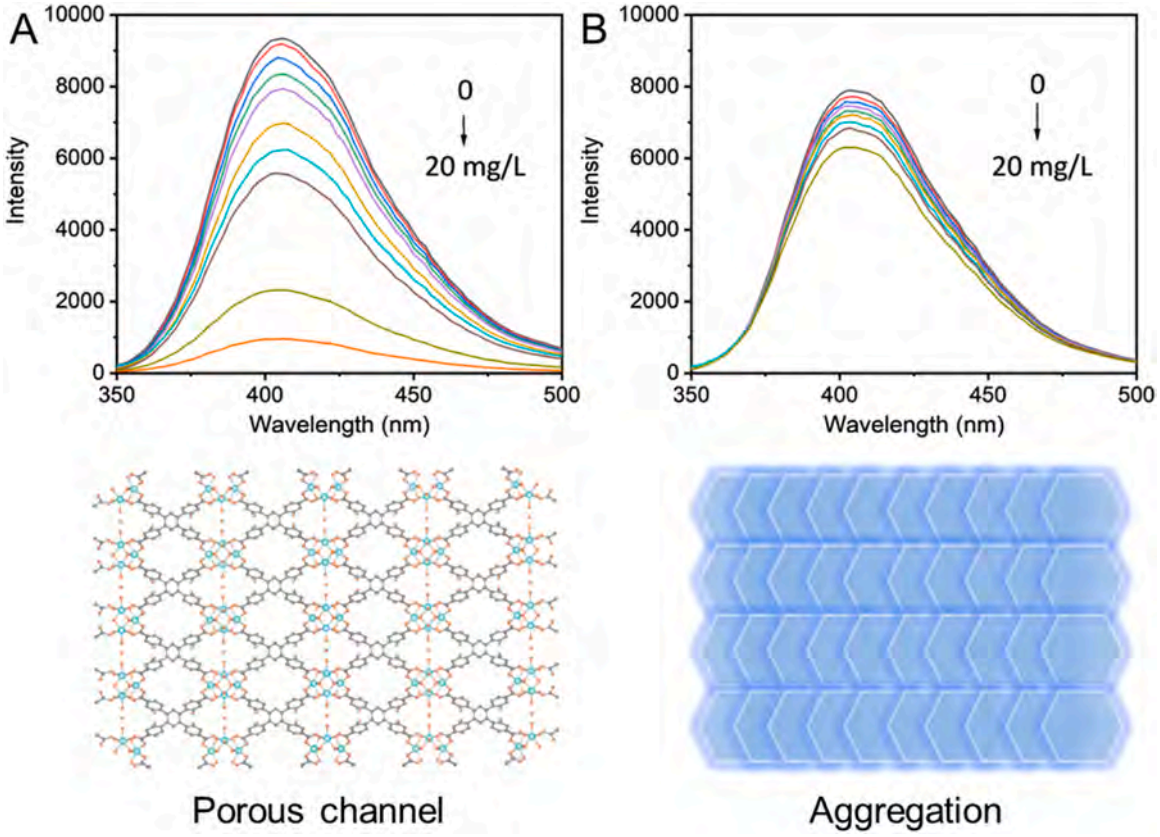

Fig. 6. Fluorescence spectra of the LMOF with different concentrations of methyl parathion and illustration of the porous channel of the LMOF (A). Fluorescence spectra of the H4TCPB with different concentrations of methyl parathion and illustration of the aggregation state of H4TCPB (B).

porous framework.

4. Conclusions

In this study, we successfully synthesized a TOCNF/LMOF hybrid material using an *in situ* synthesis approach. The nanoscale dimensions and fibrous shape of TOCNF are favorably compatible with the AIE-based LMOF particles. The integration of the TOCNF with the LMOF enabled the fabrication of materials with tailored macroscale architectures. The TOCNF/LMOF hybrids were shaped into 2D pad prototypes and exhibited a distinctive blue fluorescence under UV light exposure. These hybrid pads were developed as a portable sensing platform for the detection of methyl parathion. The sensing mechanism of the pad is based on fluorescence quenching, where its intensity decreased in the presence of methyl parathion, allowing for a quantitative measurement of the pesticide's concentration through the detection of fluorescence intensity. Our TD-DFT calculations provide insight into this quenching mechanism, suggesting that methyl parathion's fluorescence quenching occurred due to electron withdrawal from H4TCPB during excitation. Notably, the sensing capabilities of the LMOF were significantly enhanced compared to the H4TCPB ligand alone. This improvement was attributed to the LMOF's porous framework, which facilitated more extensive interactions with the methyl parathion analyte.

CRediT authorship contribution statement

Zhongyang Cheng: Formal analysis, Data curation, Writing – review & editing. **Mi Li:** Writing – original draft, Supervision, Methodology, Funding acquisition, Formal analysis, Data curation, Conceptualization. **Thomas Elder:** Writing – review & editing, Formal analysis, Data curation. **Kailong Zhang:** Writing – original draft, Methodology, Formal analysis, Data curation, Conceptualization. **Ke Zhan:** Data curation, Formal analysis. **Yucheng Peng:** Data curation, Formal analysis.

Declaration of Competing Interest

The authors declare that they have no known competing financial interests or personal relationships that could have appeared to influence the work reported in this paper.

Data Availability

Data will be made available on request.

Acknowledgements

This work was supported by the USDA National Institute of Food and Agriculture, Hatch project 7005828, South-eastern Regional Sun Grant Centre at the University of Tennessee, University of Tennessee Graduate Student Research Awards, and the US EPA's P3 program SU84087101. The BET work, performed at Auburn University, was supported by the Alabama Agricultural Experiment Station and the Hatch program of the National Institute of Food and Agriculture, U.S. Department of Agriculture ALA031-1-19091. Electron microscopy and X-ray diffraction instrument access are provided by the Institute for Advanced Materials & Manufacturing at the University of Tennessee, Knoxville. The computation for this work was performed on the University of Tennessee Infrastructure for Scientific Applications and Advanced Computing computational resources.

Appendix A. Supporting information

Supplementary data associated with this article can be found in the online version at doi:10.1016/j.jece.2024.112670.

References

[1] K. Jaga, C. Dharmani, Methyl parathion: an organophosphate insecticide not quite forgotten, Rev. Environ. Health 21 (1) (2006) 57–68.

[2] S. Garcia, A. Abu-Qare, W. Meeker-O'Connell, A. Borton, M. Abou-Donia, Methyl parathion: a review of health effects, J. Toxicol. Environ. Health B Crit. Rev. 6 (2) (2003) 185–210.

[3] S. Mukherjee, R.D. Gupta, Organophosphorus nerve agents: types, toxicity, and treatments, J. Toxicol. 2020 (2020).

[4] Af.T. Substances, D. Registry, Toxicological profile for methyl parathion, ATSDR Atlanta, Georgia, USA, 2001.

[5] O.P. Luzardo, M. Almeida-González, N. Ruiz-Suárez, M. Zumbado, L.A. Henríquez-Hernández, M.J. Meilán, M. Camacho, L.D. Boada, Validated analytical methodology for the simultaneous determination of a wide range of pesticides in human blood using GC–MS/MS and LC–ESI/MS/MS and its application in two poisoning cases, Sci. Justice 55 (5) (2015) 307–315.

[6] Z. Liang, A.M. Abdelshafy, Z. Luo, T. Belwal, X. Lin, Y. Xu, L. Wang, M. Yang, M. Qi, Y. Dong, Occurrence, detection, and dissipation of pesticide residue in plant-derived foodstuff: A state-of-the-art review, Food Chem. 384 (2022) 132494.

[7] H. Furukawa, K.E. Cordova, M. O'Keeffe, O.M. Yaghi, The chemistry and applications of metal-organic frameworks, Science 341 (6149) (2013) 1230444.

[8] L. Wang, G. Fan, X. Xu, D. Chen, L. Wang, W. Shi, P. Cheng, Detection of polychlorinated benzenes (persistent organic pollutants) by a luminescent sensor based on a lanthanide metal–organic framework, J. Mater. Chem. A 5 (11) (2017) 5541–5549.

[9] J. Liang, M.Y. Zulkifli, S. Choy, Y. Li, M. Gao, B. Kong, J. Yun, K. Liang, Metal–organic framework–plant nanobiohybrids as living sensors for on-site environmental pollutant detection, Environ. Sci. Technol. 54 (18) (2020) 11356–11364.

[10] B. Jie, H. Lin, Y. Zhai, J. Ye, D. Zhang, Y. Xie, X. Zhang, Y. Yang, Mechanism, design and application of fluorescent recognition based on metal organic frameworks in pollutant detection, Chem. Eng. J. 454 (2023) 139931.

[11] J. Dong, P. Shen, S. Ying, Z.-J. Li, Y.D. Yuan, Y. Wang, X. Zheng, S.B. Peh, H. Yuan, G. Liu, Aggregation-induced emission-responsive metal–organic frameworks, Chem. Mater. 32 (15) (2020) 6706–6720.

[12] J. Mei, Y. Hong, J.W. Lam, A. Qin, Y. Tang, B.Z. Tang, Aggregation-induced emission: the whole is more brilliant than the parts, Adv. Mater. 26 (31) (2014) 5429–5479.

[13] Z. Hu, G. Huang, W.P. Lustig, F. Wang, H. Wang, S.J. Teat, D. Banerjee, D. Zhang, J. Li, Achieving exceptionally high luminescence quantum efficiency by immobilizing an AIE molecular chromophore into a metal–organic framework, Chem. Commun. 51 (15) (2015) 3045–3048.

[14] S. Xie, Q. Liu, F. Zhu, M. Chen, L. Wang, Y. Xiong, Y. Zhu, Y. Zheng, X. Chen, AIE-active metal–organic frameworks: Facile preparation, tunable light emission, ultrasensitive sensing of copper (II) and visual fluorescence detection of glucose, J. Mater. Chem. C. 8 (30) (2020) 10408–10415.

[15] J. Tang, X. Ma, J. Yang, D.-D. Feng, X.-Q. Wang, Recent advances in metal–organic frameworks for pesticide detection and adsorption, Dalton Trans. 49 (41) (2020) 14361–14372.

[16] B.-C. Chen, C.-Q. Xiao, J.-J. Hu, Y. Peng, H.-R. Wen, S.-J. Liu, Synthesis and Structure of an Aqueous Stable Europium-Based Metal–Organic Framework with Ratiometric Fluorescence Sensing for Phosphate and Luminescence Quenching for Salicylaldehyde, Inorg. Chem. 62 (16) (2023) 6255–6262.

[17] P. Falcaro, R. Ricco, C.M. Doherty, K. Liang, A.J. Hill, M.J. Styles, MOF positioning technology and device fabrication, Chem. Soc. Rev. 43 (16) (2014) 5513–5560.

[18] M. Kalaj, K.C. Bentz, S. Ayala Jr, J.M. Palomba, K.S. Barcus, Y. Katayama, S. M. Cohen, MOF-polymer hybrid materials: From simple composites to tailored architectures, Chem. Rev. 120 (16) (2020) 8267–8302.

[19] M.L. Kim, E.H. Otal, J.P. Hinestroza, Cellulose meets reticular chemistry: interactions between cellulosic substrates and metal–organic frameworks, Cellulose 26 (2019) 123–137.

[20] A. Isogai, T. Saito, H. Fukuzumi, TEMPO-oxidized cellulose nanofibers, Nanoscale 3 (1) (2011) 71–85.

[21] H.N. Abdelhamid, A.P. Mathew, Cellulose–metal organic frameworks (CelloMOFs) hybrid materials and their multifaceted Applications: A review, Coord. Chem. Rev. 451 (2022) 214263.

[22] X.-F. Zhang, Z. Wang, M. Ding, Y. Feng, J. Yao, Advances in cellulose-metal organic framework composites: preparation and applications, J. Mater. Chem. A 9 (41) (2021) 23353–23363.

[23] T. Saito, S. Kimura, Y. Nishiyama, A. Isogai, Cellulose nanofibers prepared by TEMPO-mediated oxidation of native cellulose, Biomacromolecules 8 (8) (2007) 2485–2491.

[24] T. Saito, A. Isogai, TEMPO-mediated oxidation of native cellulose. The effect of oxidation conditions on chemical and crystal structures of the water-insoluble fractions, Biomacromolecules 5 (5) (2004) 1983–1989.

[25] M. Lammert, H. Reinsch, C. Murray, M. Wharmby, H. Terraschke, N. Stock, Synthesis and structure of Zr (iv)-and Ce (iv)-based CAU-24 with 1, 2, 4, 5-tetrakis (4-carboxyphenyl) benzene, Dalton Trans. 45 (47) (2016) 18822–18826.

[26] M. Levitus, Tutorial: measurement of fluorescence spectra and determination of relative fluorescence quantum yields of transparent samples, Methods Appl. Fluoresc. 8 (3) (2020) 033001.

[27] H. Li, C. Su, N. Liu, T. Lv, C. Yang, Q. Lu, C. Sun, X. Yan, Carbon Dot-Anchored Cobalt Oxyhydroxide Composite-Based Hydrogel Sensor for On-Site Monitoring of Organophosphorus Pesticides, ACS Appl. Mater. Interfaces 14 (47) (2022) 53340–53347.

[28] C.R. Marshall, S.A. Staudhammer, C.K. Brozek, Size control over metal–organic framework porous nanocrystals, Chem. Sci. 10 (41) (2019) 9396–9408.

[29] Y. Bai, Y. Dou, L.-H. Xie, W. Rutledge, J.-R. Li, H.-C. Zhou, Zr-based metal–organic frameworks: design, synthesis, structure, and applications, Chem. Soc. Rev. 45 (8) (2016) 2327–2367.

[30] J. Pascual-Colino, B. Artetxe, G. Beobide, O. Castillo, M.L. Fidalgo-Mayo, A. Isla-López, A. Luque, S. Mena-Gutiérrez, S. Perez-Yanez, The Chemistry of Zirconium/Carboxylate Clustering Process: Acidic Conditions to Promote Carboxylate-Unsaturated Octahedral Hexamers and Pentanuclear Species, Inorg. Chem. 61 (12) (2022) 4842–4851.

[31] A.D. French, Idealized powder diffraction patterns for cellulose polymorphs, Cellulose 21 (2) (2014) 885–896.

[32] T. Wu, Z. Zeng, G. Siqueira, K. De France, D. Sivaraman, C. Schreiner, R. Figi, Q. Zhang, G. Nyström, Dual-porous cellulose nanofibril aerogels via modular drying and cross-linking, Nanoscale 12 (13) (2020) 7383–7394.

[33] P. Samiyammal, A. Kokila, L.A. Pragasan, R. Rajagopal, R. Sathya, S. Ragupathy, M. Krishnakumar, V.R.M. Reddy, Adsorption of brilliant green dye onto activated carbon prepared from cashew nut shell by KOH activation: Studies on equilibrium isotherm, Environ. Res. 212 (2022) 113497.

[34] Z. Yuan, D. Meng, Y. Wu, G. Tang, P. Liang, J.H. Xin, D. Ye, Raman imaging-assisted customizable assembly of MOFs on cellulose aerogel, Nano Res (2022) 1–9.

[35] P. Liu, X. Li, X. Xu, K. Ye, L. Wang, H. Zhu, M. Wang, X. Niu, Integrating peroxidase-mimicking activity with photoluminescence into one framework structure for high-performance ratiometric fluorescent pesticide sensing, Sens. Actuators B: Chem. 328 (2021) 129024.

[36] Z. Zhou, S. Li, W. Wang, D. Ma, H. Zhao, L. Jia, Y. Jia, B. Yu, Two bis-color excited luminescent sensors of two-dimensional Cd (II)-MOFs bearing mixed ligands for detection of ions and pesticides in aqueous solutions, J. Mol. Struct. 1273 (2023) 134310.

[37] R. Zhang, L. Zhang, R. Yu, C. Wang, Rapid and sensitive detection of methyl parathion in rice based on carbon quantum dots nano-fluorescence probe and inner filter effect, Food Chem. 413 (2023) 135679.

[38] S. Liu, J. Zhou, X. Yuan, J. Xiong, M.-H. Zong, X. Wu, W.-Y. Lou, A dual-mode sensing platform based on metal–organic framework for colorimetric and ratiometric fluorescent detection of organophosphorus pesticide, Food Chem. 432 (2024) 137272.

[39] Q. Zhang, Z. Zhang, S. Xu, L. Da, D. Lin, C. Jiang, Enzyme-free and rapid visual quantitative detection for pesticide residues utilizing portable smartphone integrated paper sensor, J. Hazard. Mater. 436 (2022) 129320.

[40] X. Yan, T. Wang, H. Li, L. Zhang, H. Xin, G. Lu, Flexible aggregation-induced emission-active hydrogel for on-site monitoring of pesticide degradation, ACS nano 16 (11) (2022) 18421–18429.

[41] W.-J. Gong, R. Yao, H.-X. Li, Z.-G. Ren, J.-G. Zhang, J.-P. Lang, Luminescent cadmium (II) coordination polymers of 1, 2, 4, 5-tetrakis (4-pyridylvinyl) benzene used as efficient multi-responsive sensors for toxic metal ions in water, Dalton Trans. 46 (48) (2017) 16861–16871.

[42] M. Caricato, G.W. Trucks, M.J. Frisch, K.B. Wiberg, Oscillator strength: How does TDDFT compare to EOM-CCSD? J. Chem. Theory Comput. 7 (2) (2011) 456–466.

[43] W. Zeng, S. Gong, C. Zhong, C. Yang, Prediction of oscillator strength and transition dipole moments with the nuclear ensemble approach for thermally activated delayed fluorescence emitters, J. Phys. Chem. C. 123 (15) (2019) 10081–10086.

[44] H. Zhang, Z. Cao, W. Wu, Y. Mo, The Transition-Metal-Like Behavior of B2 (NHC) 2 in the Activation of CO: HOMO–LUMO Swap Without Photoinduction, Angew. Chem. Int. Ed. 57 (40) (2018) 13076–13081.

[45] K. Satheeshkumar, P.S. Kumar, R. Shanmugapriya, C. Nandhini, K. Vennila, K. P. Elango, Ratiometric fluorescence sensing of hypochlorite ion by dansyl hydrazine-Spectroscopic and TD-, DFT Stud., J. Mol. Struct. 1275 (2023) 134719.

[46] Y. Li, T.-S. Chu, DFT/TDDFT study on the sensing mechanism of a fluorescent probe for hydrogen sulfide: excited state intramolecular proton transfer coupled twisted intramolecular charge transfer, J. Phys. Chem. A 121 (28) (2017) 5245–5256.